Seasonal source variability of carbonaceous aerosols at the Rwanda climate Observatory

August Andersson[1], Elena N Kirillova[1,2], Stefano Decesari[2], Langley DeWitt[3], Jimmy Gasore[3,4,5], Katherine E Potter[3], Ronald G Prinn[3], Maheswar Rupakheti[6], Jean de Dieu Ndikubwimana[4], Julius Nkusi[4], Bonfils Safari[5].

[1] Department of Environmental Science and the Bolin Centre for Climate Research, Stockholm University, SE-10691 Stockholm, Sweden

[2] Institute of Atmospheric Sciences and Climate-ISAC, National Research Council of Italy, Bologna, Italy

[3] Center for Global Change Science, Massachusetts Institute of Technology, Cambridge, MA, USA

[4] Climate Secretariat, Ministry of Education, Kigali, Rwanda

[5] Physics Department, School of Physics, College of Science and Technology, University of Rwanda, Kigali, Rwanda

[6] Institute for Advanced Sustainability Studies (IASS), Potsdam, Germany

Correspondence: August Andersson (august.andersson@aces.su.se)

19 **Abstract**

20 Sub-Saharan Africa (SSA) is a global hotspot for aerosol emissions, affecting the regional climate

21 and air quality. In this paper we use ground-based observations to address the currently large

22 uncertainties in source-resolved emission estimation of carbonaceous aerosols. Ambient fine

23 fraction aerosol was collected on filters at the high altitude (2590 m.a.s.l.) Rwanda Climate

24 Observatory (RCO), a SSA background site, during dry and wet seasons in 2014 and 2015. The

25 concentrations of both carbonaceous and inorganic ion components show a strong seasonal cycle,

26 with highly elevated concentrations during the dry season. Source marker ratios, including carbon

27 isotopes, show that the wet and dry seasons have distinct aerosol compositions. The dry season is

28 characterized by elevated amounts of biomass burning products, approaching ~ 95% for

29 carbonaceous aerosols. An isotopic mass-balance estimate show that the amount of the

30 carbonaceous aerosols stemming from savanna fires may increase from $0.2\ \mu g/m^3$ in the wet season

31 up to $10\mu g/m^3$ during the dry season. Taken together, we here quantitatively show that savanna

32 fire is the key modulator of the seasonal aerosol composition variability at the RCO.

1. Introduction

Sub-Saharan Africa (SSA) currently faces major challenges for sustainable development, including industrial development, agriculture, fresh water supply, climate change, energy resources and air pollution (IPCC 2014; UNDP, 2018). Either directly, or indirectly, these challenges are linked to aerosol emissions. Aerosols offset the ongoing regional climate warming in SSA, shift monsoon and precipitation patterns, and are detrimental for air quality (IPCC 2013; WHO 2016). Ambient air pollution in SSA is estimated to cause 563.000 premature deaths annually, making it one of the main causes for mortality in the region (Bauer et al., 2019). However, the level of scientific understanding of the overall health- and climate impact is still low, owing to the complex aerosol lifecycle, where emissions, transformations and sinks are associated with large uncertainties, in particular given their vast physical and chemical complexity. A major limiting factor for improving our understanding of these effects in SSA are the limited number of in situ observations (Williams, 2007; Cais et al., 2011; Kulmala, 2018; López-Ballesteros et al., 2018).

A major source of aerosol emissions in SSA are dry season regional fires, clearly visible from space (Fig. 1). These are occasionally ignited naturally by lightning strikes, but are mainly lit by humans. There is evidence that slash-and-burn agriculture in SSA has been a common practice for thousands of years (Bird and Cali, 1998; Archibald et al., 2012). This long-term anthropogenic perturbation is a significant modulator of current ecosystem structure. A number of studies have specifically focused on characterizing emissions of aerosols and gases from African fires, e.g., the Southern African Regional Science Initiative Project (SAFARI 2000), conducted between 1999 to 2001 (Swap et al., 2003). Ground- and airborne chemical characterization from this and other campaigns suggest a rather distinct aerosol chemical composition, including elevated BC, K^+ and NO_3^- concentrations (Table 1).

Carbonaceous aerosols, often quantified as total carbon (TC), are generally divided into two main components: black carbon (BC; here we use elemental carbon (EC) to quantify the amounts of BC) and organic carbon (OC). Although overlapping to some extent, these two pools generally have distinct atmospheric lifecycles and environmental effects. Formed from incomplete combustion, sunlight-absorbing BC contributes to regional warming and is a particularly health detrimental component in air pollution (WHO 2012; WMO/UNEP 2011; IPCC 2013; Bond et al.,

63   2013). BC is chemically inert to atmospheric reactions, and thus the lifetime is mainly determined

64   by deposition. OC is also emitted from incomplete combustion (however, with different emission

65   factors) but is also of non-combustion origins and is formed in the air through secondary processes.

66   OC is thought to have an overall cooling effect on the climate (IPCC, 2013). Being more

67   chemically reactive, the OC pool to some extent has a more complex atmospheric lifecycle, with

68   continuous heterogenous chemistry, rendering the lifetime dependent on both precipitation and

69   chemical transformations. Emissions from SSA fires are expected to contribute to a significant

70   part of the global TC atmospheric burden (Liousse et al., 2015).

71   In general, the actual environmental impact of TC on SSA is poorly constrained. Bottom-up

72   emission projections suggests that the TC emissions from SSA are expected to increase rapidly

73   during the coming decades, perhaps reaching 50% of the global burden by 2030 (Liousse et al.,

74   2014). To quantify and evaluate such model predictions, as well as to characterize the overall

75   aerosol composition, it is valuable to conduct measurements at regional background sites. Dual

76   carbon isotope characterization ($\Delta^{14}C$ and $\delta^{13}C$) of TC at background sites in South and East Asia

77   and the Arctic has been shown to be a valuable tool for quantitatively constraining the emissions

78   from different sources (Gustafsson et al., 2009; Andersson et al., 2015; Sheesley et al., 2012;

79   Kirillova et al., 2014; Winiger et al., 2019).

80   In this paper we present dual carbon isotope constraints of TC, along with chemical

81   characterization of inorganic ions and different carbonaceous pools, from a study conducted at the

82   Rwanda Climate Observatory (RCO), during October 2014 to September 2015. A key objective

83   of the study was to estimate the relative contributions from major TC source categories at this

84   regionally representative site in the SSA. In particular, we investigate the source variability

85   associated with the seasonal variations between prevailing wet and dry monsoon seasons in the

86   region and the contributions from savanna fires.

87

88   ## 2. Methods and Materials

89   ### 2.1 Field site and regional meteorology

90   The sampling site, the Rwanda Climate Observatory (RCO), is located on the top of Mt. Mugogo,

91   in mountainous western Rwanda. (1.586° S, 29.566° E, 2590 m above sea level, 5 m.a.g.l.). The

station was established as a collaboration between the Massachusetts Institute of Technology (MIT, USA) and the Rwandan Government in 2013. The station is described in more detail by DeWitt et al. (2019). The station is an Advanced Global Atmospheric Gases Experiment (AGAGE) network site (for full list of instruments see http://agage.mit.edu).

The meteorology of Rwanda is governed by the East African monsoon, with peak rainfalls in in April and November. There are thus two dry seasons, December-January-February (DJF) and the main dry season June-July-August (JAA). The dry seasons in SSA are characterized by extensive biomass burning. During JJA the fires mainly occur to the south of Rwanda (Fig. 1). Savannas are the main biomes in SSA, covering ~ 65% of the landmass, and are the main source of fire emissions (Cahoon et al., 1992). Located in a highly elevated region, Rwanda is, broadly speaking, surrounded by savanna regions, except to the west, where the tropical rainforests of Africa are located.

2.2 Filter sampling

Quartz filter samples (Millpore, 150 mm diameter) were collected with a high-volume sampler operating at $30m^3\,h^{-1}$ using a $PM_{2.5}$ inlet (DH-77, Digitel Inc. Switzerland). Night-time only (1AM to 6AM) was conducted to minimize the effects of local emissions and day-time local atmospheric chemistry and to increase likelihood to capture the regional, free troposphere, signals. This strategy is supported by high temporal resolution investigations of the diurnal cycle of, e.g., BC (DeWitt et al., 2019). Each sample was collected over a period of 7 days. The samples were pre-combusted together with aluminum foil envelopes (400^oC for 5h), and were treated with special attention to minimize contamination. The samples were subsequently shipped to Stockholm University for chemical analysis and isolation for carbon isotope analysis. The samples were stored in freezers both on site and at Stockholm University. Field blanks were collected on a monthly basis. The present campaign covers the period October 2014 to September 2015. However, the period December 2014 to April 2015 is missing due to a lightning strike which damaged the instrument. Thus, this study presents results from analysis of filter samples (in total 25) collected for the periods that cover the beginning of the 2014 fall rainy season (Oct-Nov), the end of the spring 2015 rainy season (April – May) and the dry 2015 summer season (June – September). We jointly refer the October-November 2014 and the April-May 2015 periods as the wet seasons.

2.3 Concentrations analysis

The concentrations of elemental carbon (EC – mass-based tracer for black carbon) and organic carbon (OC) were determined using a Sunset Inc. (Tigard, Oregon, USA) thermal-optical instrument using the NIOSH 4050 protocol (Birch and Cary, 1996; Table S1). Pre-treatment using acid fumigation with 1M HCl ensured efficient removal of carbonates. A glucose solution was used to calibrate the FID-response of the instrument, and the long-term performance of the instrument was checked through running of National Institute of Standards and Technology (NIST) Standard Reference Materials (SRM) standards. All the concentrations were blank corrected and the field blank input was on average 2% for OC and 0% for EC. The average relative standard deviation of the triplicate analysis was 5% for OC, 7% for EC.

Water-soluble organic carbon (WSOC) was extracted from filter sub-samples in ultra-pure Milli-Q water by shaking for 1.5 hours. The extracts were filtered using 0.45 µm cutoff PTFE syringe filters (Minisart-SRP 10, Sartorius Stedim Biotech, Germany). The concentration of WSOC was quantified in the filtered solutions as the difference between total water-soluble carbon and water-soluble inorganic carbon using a high temperature catalytic oxidation instrument TOC-5000A (Shimadzu, Japan). The samples were neither acidified nor purged, to avoid the loss of volatile organic compounds. The accuracy of the measurement ranges from 7% (70 µg L^{-1}) for 1 mg L^{-1} of carbon solution to 3% for concentrations higher than 2 mg L^{-1} of carbon (corresponding to 60 µg L^{-1}). All the measurements were blank corrected. WSOC field blanks corresponded to an average 0.5%. The average relative standard deviation of the triplicate analysis was 10%.

The concentrations of water-soluble inorganic anions were determined by ion chromatography using a Dionex ICS-2000 system. Anions were separated using an IonPac AG11 2x50 mm Dionex guard column, IonPac AS11 2x250 mm Dionex separation column and ASRS 300 self-regenerating suppressor. A solution of KOH was used as eluent. Cations were separated using an IonPac CG16 3x50 mm Dionex guard column, IonPac CS11 3x250 mm Dionex separation column and CSRS 300 self-regenerating suppressor. The analysis of cations was performed using 30 mM solution of MSA as eluent. Field blanks constituted on average 3% of NO_3^-, 2% of SO_4^{2-} and 1% of NH_4^+ and K^+ ion concentrations. The triplicate analysis showed the average relative standard deviation of 2% for NO_3^- and K^+, 5% for SO_4^{2-} and 6% for NH_4^+.

151

152   2.4 Isotope analysis

153 Approximately every second sample (n = 12) were selected for carbon isotope ($\Delta^{14}C$ and $\delta^{13}C$)

154 analysis of total carbon (TC = OC + EC; Table S1). The filter samples were combusted using the

155 Sunset analyzer (total carbon protocol) and the evolved CO_2 was collected in glass vials using a

156 liquid nitrogen cryo-trap (Andersson et al., 2015). The vials were subsequently shipped to the

157 National Ocean Sciences Accelerator Mass Spectrometry (NOSAMS) facility at the Woods Hole

158 Oceanographic Institute (Falmouth, Massachusetts, USA) for analysis of the dual carbon isotope

159 signatures. The $\Delta^{14}C$-signature was measured using accelerator mass spectrometry (AMS), while

160 the $\delta^{13}C$-signature was measured using an Isotope Ratio Mass Spectrometer (IRMS).

161

162   2.5 Source Apportionment

163 The $\Delta^{14}C$-signature allows the differentiation between the relative contributions of

164 biogenic/biomass burning and fossil sources. The fraction biogenic/biomass burning (f_{bio}) may be

165 calculated using isotopic mass-balance ($f_{fossil} = 1 - f_{bio}$):

166   $f_{bio} = \dfrac{\Delta^{14}C_{sample} - \Delta^{14}C_{fossil}}{\Delta^{14}C_{bio} - \Delta^{14}C_{fossil}}$ (1)

167 The fossil endmember is -1000‰, as it is completely depleted in ^{14}C. The biomass endmember is

168 more complex. For annual plants it is fairly straight-forward: the biomass $\Delta^{14}C$-signature equals

169 the $\Delta^{14}C$ value of CO_2 for that year (~ +20‰ for 2014/15, Graven, 2015; Turnbull et al., 2017).

170 For more long-lived species (e.g., trees) the $\Delta^{14}C$-signature is the average of the atmospheric CO_2

171 values (weighted by yearly carbon accumulation) over the plants' lifetime. Bottom-up estimation

172 of $\Delta^{14}C_{bio}$ therefore requires information regarding the plant distribution in the area of interest, and

173 the annual bioaccumulation of carbon for the different plants. As an alternative we here use the

174 combined $\Delta^{14}C$-signature of dissolved organic carbon (DOC) in three of the regions' major rivers,

175 Congo, Zambezi and Tana, to obtain a regional $\Delta^{14}C_{bio} = +57 \pm 52$ ‰, which is well in the expected

176 range of a mixture of annual and multi-year plants (Marwick et al., 2015; Wild et al., 2019, Winiger

177 et al., 2019).

178 The vegetation in SSA may be divided into two main photosynthetic classes: C_3-plants and C_4-

179 plants, see discussion in Section 3.5. These two groups have distinct $\delta^{13}C$-signatures, allowing

180 isotope-based separation. We may then resolve three source classes by combining $\Delta^{14}C$ and $\delta^{13}C$:

181 C_3-plants, C_4- plants and fossil, through isotopic mass-balance (Andersson et al., 2015):

182
$$\begin{pmatrix} \Delta^{14}C(i) \\ \delta^{13}C(i) \\ 1 \end{pmatrix} = \begin{pmatrix} \Delta^{14}C_{C3} & \Delta^{14}C_{fossil} & \Delta^{14}C_{C4} \\ \delta^{13}C_{C3} & \delta^{13}C_{fossil} & \delta^{13}C_{C4} \\ 1 & 1 & 1 \end{pmatrix} \begin{pmatrix} f_{C3}(i) \\ f_{fossil}(i) \\ f_{C4}(i) \end{pmatrix} \qquad (2)$$

183 Endmember variability may significantly influence the calculated source fractional contributions

184 (Andersson, 2011). For a discussion on the specific endmember ranges used here, see Section 3.5.

185 In Eq. (2) the isotopic data is treated as independent. However, here we find that there is a

186 dependence between the isotope ratios and the TC concentrations, such that $\Delta^{14}C(i) \sim A/TC(i) +B$,

187 where A and B are constants, and i is the sample index (Fig. 5). This is known as a Keeling relation,

188 and is discussed in more detail in Section 3.4. The relation holds for both $\Delta^{14}C$ ($R^2=0.85$, $p<0.01$)

189 and $\delta^{13}C$, while the correlation is weaker for $\delta^{13}C$ ($R^2=0.55$, $p<0.1$). A method for using

190 correlations within the framework Bayesian source apportionment has recently been developed

191 (Martens et al., 2019). The rationale is based on both statistical concepts and the averaging

192 expected from atmospheric mixing. The endmember ranges used in the calculations are from

193 isolated sources, but during long-range transport the variability within a given source, e.g., savanna

194 fires, will be reduced. Using correlations between data points, a means for accounting for the

195 mixing is obtained, and more realistic source fraction estimates are obtained. When using the

196 estimated source fractions to back-calculate the isotope signatures, the agreement is good

197 compared with direct fits (Fig. 5 and Fig. S2). A sensitivity analysis is discussed in section 3.5

198 (Fig. S3)

199 To account for the correlations in the data-set we therefore add a second constraint in the source

200 apportionment calculations, based on the relation to the TC concentrations:

201
$$\begin{pmatrix} f_{C3}(i) \\ f_{fossil}(i) \\ f_{C4}(i) \end{pmatrix} = \frac{1}{[TC(i)]} \cdot \begin{pmatrix} f_{C3,slope} \\ f_{fossil,slope} \\ f_{C4,slope} \end{pmatrix} + \begin{pmatrix} f_{C3,intercept} \\ f_{fossil,intercept} \\ f_{C4,intercept} \end{pmatrix} \qquad (3)$$

202 Where we, instead of fitting a source vector (f_{C3}, f_{fossil}, f_{C4}) for each individual data pair, fit two

203 vectors: a slope and an intercept of the line, to all data points. This clearly holds the advantage of

204 have fewer fitting parameters. We emphasize that the strength of the correlation of the isotope

205 signatures relative to 1/TC is naturally incorporated into this relation, such that lower correlation

206 of δ^{13}C w.r.t 1/TC impose weaker constraints on the calculated source fractions, compared to Δ^{14}C.

207 The source fractions were computed using numerical Markov chain Monte Carlo simulations,

208 implemented in Matlab, ver. 2015b, using 1000.000 iterations with a burn-in (initial search phase)

209 of 10.000 and a data thinning of 10 (removing step-wise correlations). The stochastic perturbation

210 parameter was adjusted as to obtain an acceptance ratio of 0.23, which has been suggested to be

211 optimal for Metropolis-Hastings algorithms (Roberts et al., 1997). For this set-up, the variability

212 in the numerically estimated parameters, e.g., the standard deviation of the relative source fraction,

213 is lower than 1% of the mean value, suggesting good convergence (Winiger et al., 2017).

214

215 2.6 Air Mass Back trajectories and Remote Sensing

216 10-days air mass back-trajectories (arrival height 2690 m.a.s.l. (100 m.a.g.l.) and 3090 m.a.s.l.

217 (500 m.a.g.l.) were calculated using the NOAA Hybrid Single Particle Lagrangian Integrated

218 Trajectory Model (HYSPLIT) (Figs. 1 and S1). Remote sensing fire-spot detections were retrieved

219 from the NASA Fire Information for Resource Management Services (FIRMS) database, based on

220 retrievals from the Moderate Resolution Imaging Spectroradiometer (MODIS) satellite product.

221

222 **3 Results and Discussion**

223 3.1 Back-trajectory analysis

224 Air mass back-trajectory analysis show that the air masses arriving at the Rwanda Climate

225 Observatory (RCO) during the filter collection periods are overall easterly/southeasterly (Figs. 1

226 and S1). There is some overlap between the wet and boreal summer dry seasons, but overall there

227 is a seasonal switch, where the wet seasons air masses are more of directly eastern origins (e.g.,

228 Uganda and Kenya and Tanzania), whereas the dry are more directly southeastern (e.g., Burundi,

229 Tanzania and Democratic Republic of Congo). During the dry season there are extensive fires to

230   the south of RCO, mainly to the south-west (DR of Congo and Angola). However, the air masses

231   also pass over regions with comparably high fire activities in the southeast, mainly in Tanzania.

232   Nevertheless, we emphasize that back-trajectory analysis is challenging in mountainous regions

233   (e.g., Winiger et al., 2019), and the actual geographical footprints are expected to be broader, e.g.,

234   due to the propagating effects of turbulence. Here we interpret the back-trajectories qualitatively

235   to visualize overall air mass transport patterns.

236

237   3.2 Concentrations of fine aerosol components

238   During the present campaign, the $PM_{2.5}$ carbonaceous and inorganic ion components show a strong

239   seasonal variability, with elevated levels during the dry JJA season (Fig. 2, Table S1). The dry/wet

240   season ratios for TC, EC, WSOC, NO_3^-, SO_4^{2-}, NH_4^+ and K^+, were 4.2, 7.0, 4.1, 12.6, 3.0, 3.2 and

241   8.8, respectively (Table 1). This variability suggests differences in the aerosol sources and

242   atmospheric processing, in addition to seasonality in meteorology, e.g., varying boundary layer

243   heights or precipitation. The sea-salt contributions to the ions are overall estimated to be less than

244   1%, using corrections with sodium ions (Blanchard and Woodcock, 1980). We here report the

245   actual concentrations to facilitate direct comparisons with previous studies (Table 1). Overall,

246   these differences reflect differences in aerosol atmospheric lifetime, air mass transport pathways

247   and emissions seasonality (e.g., fires). Elevated ratios of EC and K^+ suggests an increased

248   influence from biomass burning during the dry season. NO_3^-, which displays the largest seasonal

249   shift, is often associated with oxidized NO_x from traffic emissions or lightning strikes. However,

250   it is also typically elevated in emissions from savanna fires (Table 1; e.g., Gao et al., 2003;

251   Formenti et al., 2003).

252   The dry season concentrations of carbonaceous aerosols components and inorganic ions reported

253   here are overall in good agreement with the concentrations observed dry season rural and aged

254   savanna fire air masses (Table 1). The BC values are in the same range as has previously been

255   observed at Mt. Kenya (0.72 ± 0.06 μgC m^{-3}, Gatari et al., 2003). During atmospheric aging of a

256   biomass plume, the values of OC, EC and K^+ decrease by a factor of 2-3, whereas other

257   components are relatively unaffected (Table 1). However, the effects appear variable, as compared

258   with savanna fires in South Africa (Gao et al., 2003).

259 RCO is situated not far away from the Nyiargongo and Nyamuragria Volcanoes in eastern
260 Democratic Republic of Congo. High spatial resolution ($13x24km^2$) satellite-monitoring of the
261 SO_2 levels show a near-constant emissions from these volcanoes over the time period covering the
262 present campaign, likely affecting the observed sulfate levels (Barrière et al., 2017). Here we
263 observe a spike in sulfate levels (~ 5μg m^{-3}) during the week starting of the 13th of June 2015 (Fig.
264 2), but with no clear linkage to an increase in volcanic SO_2 emissions.

265

266 3.3 Source marker ratios and correlations

267 Overall, the ratios of different aerosol components provide insights into sources or atmospheric
268 processes. Here, the EC/TC shows a distinct seasonality (Fig. 3 and Table S1). More commonly
269 analyzed, though, is the OC/EC ratio (=(TC-EC)/EC), with elevated levels during the wet season
270 (11±3) compared to the dry season (7±3; Table S1). The OC/EC-ratio is sometimes used as a
271 marker for biomass burning, but is highly influenced by burning conditions such as flaming or
272 smoldering fires. In addition, it is highly influenced by atmospheric processes such as secondary
273 organic aerosol (SOA) formation or photo-chemical aging (e.g., Dasari et al., 2019). The dry
274 season values observed here are similar to what has been observed in background air at other dry
275 season Sub-Saharan African sites (Table 1).

276 Similarly, the NH_4^+/TC and SO_4^{2-}/TC are also elevated during the wet seasons (Fig. 3), while
277 decreasing during the dry seasons, suggesting a different source profile compared to EC, K^+ and
278 NO_3^-, including potential volcanic input of SO_2. In contrast, the WSOC/OC-ratio shows no clear
279 seasonality, indicating small differences in sources and atmospheric processing of water-soluble
280 and water-insoluble organic components over the year. TC correlates with K^+ ($R^2 = 0.95$, p<0.01)
281 and NO_3^- ($R^2 = 0.95$, p<0.01), suggesting that the incomplete combustion regime during the present
282 campaign is governed by biomass emissions, e.g., savanna burning. Taken together, these ratios
283 qualitatively suggest that the aerosol regime at RCO is strongly influenced by occasional input of
284 biomass burning products during the boreal dry season.

285

286 3.4 Carbon isotopes

287   Radiocarbon ($\Delta^{14}C$) and stable-carbon ($\delta^{13}C$) provides detailed information regarding the sources

288   and atmospheric processing of carbonaceous aerosols. Here, we investigated the signatures of TC

289   for roughly every second sample during the campaign. The $\Delta^{14}C$-marker is not influenced by

290   atmospheric processing, and may be used to directly compute the relative contributions of fossil

291   vs biomass/biogenic sources with high precision, Eq. (1). The $\Delta^{14}C$-signature show an oscillation

292   over the seasons, ranging between -84‰ (November, 2014) and +30‰ (July, 2015) (Fig. 4 and

293   Table S1). Thus, during the JJA season, the $\Delta^{14}C$-signature exceed the signature for atmospheric

294   CO_2 (+20‰, Graven, 2015; Turnbull, 2017).

295   Using Equation (1), the percentage biomass/biogenic TC for the $\Delta^{14}C$ = +30‰ sample is 97%.

296   During the wet season, the percentage derived from fossil reaches 13%, possibly of a more local

297   derivation. $\Delta^{14}C$ correlates with 1/TC (R^2 = 0.85, p<0.01), which suggests that the variability in

298   concentrations can be explained as a two-component mixture: a stable background and a

299   temporally fluctuating source (Keeling, 1958) (Fig. 5A). This inverse relation gives $\Delta^{14}C$ = +37 ±

300   6‰ as TC approaches infinity, showing that the non-background component is of

301   biogenic/biomass burning origins. The $\Delta^{14}C$ signatures for TC reported here are overall higher

302   than for monitoring sites in South and East Asia (Sheesley et al., 2012; Kirillova et al., 2014;

303   Bikkina et al., 2016).

304   In contrast to $\Delta^{14}C$, the $\delta^{13}C$-value is influenced by both atmospheric processes (i.e., kinetic isotope

305   effects, KIE) and source signatures. Here, the $\delta^{13}C$-value shows a similar pattern relative to the

306     $\Delta^{14}C$-value, depleted in ^{13}C (min $\delta^{13}C$ = -27‰) during wet seasons, and higher during the dry

307   season (max $\delta^{13}C$ = -21 ‰) (Fig. 4B). The correlation w.r.t. 1/TC (R^2=0.55, p<0.1) is weaker

308   compared to $\Delta^{14}C$ (Fig. 5B). The direct fossil vs biomass source correlation from the $\Delta^{14}C$ Keeling

309   curve is also driving the $\delta^{13}C$-signatures, but the higher variability is explained by larger

310   endmember variability and potential influence of KIE, see Section 3.5. An overall enrichment in

311   ^{13}C has been found in aged air masses in South Asia, especially for WSOC (Kirillova et al., 2013;

312   Dasari et al., 2019), but less so for TC. In fact, the enrichment of ^{13}C in WSOC often appears to

313   be counter-acted by a decrease in water-insoluble OC (e.g., Yan et al., 2017; Fang et al., 2017).

314   The TC $\delta^{13}C$ values, and their seasonal trend, are similar to what has previously observed in fine

315   aerosols at a rural site in Tanzania (May – August, 2011, Mkoma, et al., 2014). However, the

316 temporal trend appears shifted in the RCO samples from values around -25 ‰ to around 22 ‰ in

317 mid-May. At the Tanzanian site, a similar shift occurs in mid-June. In addition to the complications

318 of comparing measurements conducted at different sites during different years, there is a good

319 agreement in the δ^{13}C-values, and the temporal offset may be explained by inter-tropical

320 convergence zone position variability. Similarly, the δ^{13}C-value for TC at a savanna woodland site

321 in Zambia, observed during August-September 2000, was -21.8±0.8 ‰ (Billmark et al., 2003),

322 while values between -19.3 and –23.6 ‰ were observed at sites in the Ivory Coast (Cachier et al.,

323 1985).

324 3.5. Carbon isotope-based source apportionment

325 By combining the Δ^{14}C and the δ^{13}C-values we can by isotopic mass balance resolve three major

326 sources of TC at the RCO, Eq. (2). However, there are some important considerations to this

327 approach: First, the δ^{13}C-value is not an exclusive source marker, but is also affected by

328 atmospheric processing (e.g., photo-chemical oxidation and secondary formation). Second, the

329 main source categories must be defined and distinguishable using carbon isotopes. Third, the

330 source-values of the isotope-signatures, the endmembers, and their natural variability need to be

331 established.

332 As mentioned, the δ^{13}C-value of bulk TC appears to be considerably less affected by atmospheric

333 processing compared to sub-components, such as WSOC. Here, the temporal variation of the δ^{13}C-

334 value is qualitatively similar to that of Δ^{14}C-value (Fig. 4). Since Δ^{14}C is not affected by

335 atmospheric reactions, this suggests that source variability is a key driver of the δ^{13}C variability.

336 Furthermore, the WSOC/OC is virtually constant throughout the year (Fig. 3); the WSOC/OC has

337 been found to be highly affected by atmospheric processing and related to shifting δ^{13}C (Kirillova

338 et al., 2013; Yan et al., 2017; Fang et al., 2018; Dasari, 2019). Here, we therefore assume that the

339 δ^{13}C-ratio of TC is not strongly perturbed by atmospheric processing during long-range transport,

340 and may thus be used as a source marker. Nevertheless, we explore the potential influence on KIE,

341 as well as endmember variability, on the source apportionment results in a sensitivity analysis.

342 Turning to potential sources, there is a multitude of potential source categories for TC in SSA.

343 However, many of these falls in broad categories, with similar carbon isotope signatures. Around

344 the world, the applications of dual carbon isotope source apportionment techniques in ambient TC

345   mainly identified/considered 6 broad source categories: C_3 plants, C_4 plants, liquid fossil fuels

346   (e.g., traffic), coal combustion (solid fossil), gas flaring (gaseous fossil) and marine emissions

347   (Winiger et al., 2019; Andersson et al., 2015; Kirillova et al., 2013). Overall, the practice of coal

348   combustion in SSA is expected to be much less frequent than in, for example, South and East Asia,

349   and we therefore do not consider this source further. In addition, marine emissions are not expected

350   to have a large influence at RCO, supported by the low estimates of marine contributions to the

351   inorganic ions (<1%). For gas flaring, there are potential distant sources around the Arabian

352   Peninsula and off the west coast of Africa, in the Gulf of Guinea. However, given the distances to

353   the RCO station and the prevailing wind directions, emissions from flaring are not expected to

354   affect the site, while the $\delta^{13}C$-signatures for gas-flaring are strongly depleted in ^{13}C ($\delta^{13}C<-38‰$;

355   Winiger et al., 2017) and even a small contribution would shift the observed values significantly.

356   The remaining three main source categories are the two biomass sources of C_3 (e.g., trees) and C_4

357   plants (e.g., sugarcane and certain grasses) and liquid fossil fuels (Fig. 6). Aerosols from liquid

358   fossil fuel sources have a $\Delta^{14}C_{fossil}$ = -1000‰ (completely depleted in ^{14}C) and a $\delta^{13}C_{fossil}$ = -

359   25.5±1.3‰ (Widory, 2006; Andersson et al., 2015). The $\Delta^{14}C$ of biomass was established in

360   Section 2.4 as $\Delta^{14}C_{C3} = \Delta^{14}C_{C4} = +57 \pm 52‰$. The $\delta^{13}C$ of C_3-plants in general is -27.1±2‰

361   (Bender, 1971; O'Leary, 1988). However, for aerosols generated from C_3-plants this value may be

362   either enriched (e.g., ~ 0.5‰ biomass burning) or depleted (e.g., ~ 0 to 4‰ during SOA formation)

363   (Turekian, 1998; Das et al. 2010, Mkoma et al., 2014; Aguilera and Whigham, 2018). In any case,

364   the numerical spread in the $\delta^{13}C$-value of these different sources are largely overlapping with that

365   of the raw materials, and we therefore use this value here. The $\delta^{13}C$ of C_4-plant materials is -

366   13.1±1.2‰ (Bender, 1971; O'Leary, 1988; Turekian 1998). However, during incomplete

367   combustion, the $\delta^{13}C_{C4}$ may be reduced by a factor ranging from 0 to 7‰, largely dependent on

368   burning conditions and species (Martinelli, 2002; Das et al., 2010; Aguilera and Whigham, 2018).

369   Accounting for such effects in source apportionment is a challenge, especially since the reported

370   values are ranges and not mean and variability, and thus are highly influenced by potential outliers.

371   We here use a method discussed in Andersson et al. (2015) to address the issue of statistical

372   analysis of ranges by assuming that the total range corresponds to the 95% confidence intervals of

373   a normal distribution. This corresponds to the range of 4 times the standard deviation, yielding σ

374   = 7/4‰, while the mean is -7/2‰. Combining this with the variability of the of pure C_4-plants we

375 obtain: $\delta^{13}C_{C4}$: -16.6 ± 2.2‰, where $\sigma^2 = 1.2^2 + (7/4)^2$ ‰^{2}. These values are also what is obtained

376 by numerical estimation of the convolution of a normal distribution (μ = -16.6‰, σ = 1.2‰) with

377 a uniform distribution ([-7, 0] ‰), adding to the strength of statistical representation.

378 The fractional source contributions of fossil fuel, C_3 and C_4 to TC are computed with Eqs. (2) and

379 (3) (Fig. 7). It is well-established that accurate estimation of the fractional source contributions

380 requires explicit incorporation of the endmember variability, and we here use a Bayesian

381 framework driven by Markov chain Monte Carlo simulations for this purpose (Andersson, 2011;

382 Andersson et al., 2015). To estimate the influence of the intra-endmember mixing during

383 atmospheric transport we use the correlations of the isotopes with TC within the Bayesian

384 framework, see section 2.5, to account for the endmember averaging during atmospheric transport

385 (Martens et al., 2019) (Fig. 5). The resulting fractional contributions display a large variability

386 when comparing wet and dry conditions (Fig. 7A and Table S2). The dry season is characterized

387 by relatively higher C_4-plant contributions, whereas the relative contributions of fossil fuels and

388 C_3-plants increase during the wet seasons. Back-calculating the isotope signatures from the

389 computed source fractions from the MCMC-simulations essentially reproduce the Keeling

390 relations relative to 1/TC (Figs. 5 and S2). To check influence of the number of data points used

391 in the Keeling-based MCMC, we computed comparative scenarios where every third data point

392 was used (starting at data point 1, 2 and 3 respectively) (Fig S3). The standard deviations for the

393 calculated f_{C3} are on average doubled when only every third point are used (5% vs 10%), showing

394 how correlations between multiple data points aids in constraining the sources.

395 Since the $\delta^{13}C$ endmembers for, in particularly C_4-plants, are not well-constrained, we also

396 employed a sensitivity analysis w.r.t. endmembers and the potential influence of KIE (Tables S2

397 – S5 and Figs. S4 – S6). In addition to the above discussed best estimate scenario, we tested two

398 $\delta^{13}C_{C4}$ scenarios: a 'minimum KIE scenario' with zero KIE ($\delta^{13}C_{C4}$ -13.1±1.2‰) and a 'maximum

399 KIE scenario', with a depletion by 5.9‰ ($\delta^{13}C_{C4}$ -19.0±2.2‰). The maximum KIE scenario was

400 established such as the $f_{C4}/(f_{C4}+f_{C3})$-ratio would be 62% as TC approach infinity, and thus 100%

401 savanna contributions, see Eq. (4). As expected, these scenarios significantly shift the estimated

402 relative C_4 contributions, resulting in a total range of the sample period averages of 24% (min-

403 KIE; min 6% max 32%) to 42% (max-KIE; min 10%, max 58%), thus providing lower and upper

404 bounds (Figs. S4 and S5 and Tables S3 and S4). The corresponding value for our best estimate is

405 32% (max 44%, min 8%). In addition, we investigated a scenario with a 3‰ depletion of the fossil

406 endmember ($\delta^{13}C_{fossil}$ -28.5±1.3‰). Since the fossil contribution is overall low as determined by

407 $\Delta^{14}C$, and since $\Delta^{14}C$ constrains the fossil contribution independently of the $\delta^{13}C$ data, this shift

408 has no significant influence on the computed source fractions 6% (max 11%, min 3%) (Fig. S6

409 and Table S5). Overall, we stress that these three sensitivity test scenarios represent extreme limits,

410 and the a priori least biased scenario is the initially outlined best scenario.

411 By combining the estimated fractional source contributions with the TC concentrations, we can

412 estimate the concentrations from the different sources (Fig. 7B), revealing a more accentuated

413 source variability. The average dry-to-wet ratios of the TC to C_3-plants, C_4-plants and fossil fuels

414 are 3, 5 and 2, respectively.

415 Savannas are the main biome supporting C_4-plants in SSA. For East African savannas, $\delta^{13}C$ data

416 suggests that ~ 62% ($f_{C4,NPP}$) of the net primary production (NPP) is from C_4-plants (the rest mainly

417 C_3-plants, Lloyd et al., 2008). Thus, one may assume that the source characteristics of TC emitted

418 from savanna burning should represent this plant-signature distribution. However, the aerosol

419 emissions modulate the NPP activity through emission factors (EF). The uncertainties of EFs from

420 different biomass burning activities are generally large and overlapping (Andreae, 2019). As a first

421 approximation, we here use $f_{C4,NPP}$ to estimate the fractional contribution of savanna emissions to

422 TC ($f_{savanna}$) as (i = sample index):

423 $$f_{savanna}(i) = \frac{f_{C4}(i)}{f_{C4,NPP}}$$ (4)

424 This analysis shows that the dry season carbonaceous aerosol regime is dominated by savanna fire

425 emissions reaching up to 71% (Fig. 7 and Table S2). These results agree with the elevated levels

426 of EC, K^+ and NO_3^- during the dry season (Table S1).

427

428 5. Outlook

429 In this paper we find that the aerosol composition of the emissions affecting the Rwanda Climate

430 Observatory (RCO) may be described as a two-state source mixture: a regional/local background

431 signal modulated by savanna fire emissions. Multiple studies have shown that savanna fires

432 strongly influence the aerosol regime in SSA. Here, we estimate the savanna fire contributions for

433   carbonaceous aerosols to range from 13% (wet season; $TC_{savanna} = 0.2$ μg m^{-3}) to 71% (dry season;

434    $TC_{savanna} = 9.7$ μg m^{-3}) at RCO (Fig. 7). The savanna fires are believed to be mainly lit by humans,

435   and although these activities have been ongoing perhaps throughout the Holocene, these

436   anthropogenic activities strongly perturb the regional ecosystems, climate and air quality (e.g.,

437   Bird and Cali, 1998; Archibald et al., 1998). The annual SSA savanna carbon budget represents a

438   net CO_2 source to the atmosphere (Williams, 2007; Cais et al., 2011; Valentini et al., 2014; Palmer

439   et al., 2019). Finding more sustainable alternatives to the slash-and-burn practices in SSA could

440   therefore possibly turn the region into a carbon sink. For instance, implementation of early dry

441   season burning may be a possible strategy (Lipset-Moore et al., 2018). Savanna fire mitigation

442   would also improve the regional air quality and stabilize precipitation patterns (Hodnebrog et al.,

443   2015; Heft-Neal et al., 2018; Bauer et al., 2019).

444   Nevertheless, the current level of scientific understanding of the impact of savanna burning on the

445   environmental system is poor, as are the couplings/responses to climate change, population

446   growth, urbanization and other key socio-economic and environmental challenges for sustainable

447   development in SSA (e.g., IPCC, 2014; Liousse et al., 2015; Brandt et al., 2017; UNDP, 2018).

448   Savanna burning mitigation, or shifts in in fire regime due to climate change, may change the

449   present steady-state in unpredictable ways (e.g., Abreu et al., 2017). To better constrain the

450   multiple environmental impacts of savanna burning in SSA, the comparably few ongoing ground-

451   based in situ observations should be expanded and solidified (Williams, 2007; Cais et al., 2011;

452   Kulmala, 2018; López-Ballesteros et a., 2018). For instance, observations of source-segregated

453   aerosol concentrations provides multiple opportunities for advancing our knowledge of

454   environmental processes relevant to SSA, including providing means for testing chemical-

455   transport models; examining the relative importance of cooling vs warming (e.g., BC) aerosols;

456   ground-truthing remote sensing products and detailed monitoring of the expected rapid change

457   over the coming decades, including the effects of climate warming, population growth and

458   urbanization.

459

460   *Data availability:* The chemical and isotopic data, as well as the MCMC-derived relative source

461   contributions of C_3-plants, C_4-plants and fossil, and the corresponding source-segregated TC

462   concentrations is provided in the supplementary information.

463

464   *Competing interests:* The authors declare that they have no conflict of interest.

465

466   *Author contributions*: AA wrote the manuscript, set-up the $PM_{2.5}$ high-volume sampler at RCO,
467   and analyzed the data. ENK and SD conducted the carbonaceous aerosol quantifications and
468   isolations for isotopes, and IC analysis. JG worked with the instruments, including helping or
469   leading installation, and provided feedback on data analysis. KEP was instrumental in setting up
470   the RCO and did most of the initial instrument installation. HLD served as the RCO station chief
471   scientist for three years. JN and JdDN worked as technical coordinators of the project at different
472   times and facilitated the operations of the station as well as providing feedback on analysis. BS
473   was our University of Rwanda liaison as the head of the Master's program in atmospheric and
474   climate science. RGP is the head of the AGAGE network and is the MIT liaison to the RCO, and
475   was essential in the setup of the observatory and scientific analysis. All authors commented on the
476   manuscript.

477

478   *Acknowledgement*s. We thank the generous MIT alumni donors to the MIT-Rwanda Climate
479   Observatory Project and the MIT Center for Global Change Science. We also thank the
480   Government of Rwanda and the Rwanda Ministry of Education. We also wish to acknowledge the
481   essential contributions of the Mugogo station technical experts Theobard Habineza, Modeste
482   Mugabo, Olivier Shyaka, and Gaston Munyampundu and RBA technician Yves Fidele, without
483   which running this station would be impossible. AA acknowledges project grants from the
484   Swedish Research council (projects 348-2013-114 and 2017-05687). ENK acknowledges the
485   People Programme (Marie Curie Actions) of the European Union's Seventh Framework
486   Programme (FP7/2007-2013) under REA grant agreement 623386. We acknowledge the use of
487   data and imagery from LANCE FIRMS operated by NASA's Earth Science Data and Information
488   System (ESDIS) with funding provided by NASA Headquarters. The authors gratefully
489   acknowledge the NOAA Air Resources Laboratory (ARL) for the provision of the HYSPLIT
490   transport and dispersion model and/or READY website (http://www.ready.noaa.gov) used in this
491   publication.

References

Abreu, R.C., Hoffmann, W.A., Vasconcelos, H.L., Pilo, N.A., Rossatto, D.R., Durigan, G.: The biodiversity cost of carbon sequestration in tropical savanna. Sci. Advan. 3, doi: 10.1126/sciadv.1701284, 2017.

Aguilera, J., Whigham, L.D.: Using the $^{13}C/^{12}C$ carbon isotope ratio to characterize the emission sources of airborne particulate matter: a review of literature. Isotopes Environ. Health. Stud 54, 573-587, doi: 10.1080/10256016.2018.1531854, 2018.

Andersson, A.: A systematic examination of a random sampling strategy for source apportionment calculations. Sci. Tot. Environ. 412-413, 232-238, doi: 10.1016/j.scitotenv.2011.031, 2011.

Andersson, A., Deng, J., Du, K., Zheng, M., Yan, C., Sköld, M., Gustafsson, Ö.: Regionally-varying combustion sources of the January 2013 severe haze events over Eastern China. Environ. Sci. Technol. 49, 2038-2043, doi: 10.1021/es503855e, 2015.

Andreae, M.O.: Emission of trace gases and aerosols from biomass burning – An updated assessment. Atmos. Chem. Phys. Discuss. doi: 10.5194/acp-2019-303, 2019.

Archibald, S., Staver, A.C., Levin, S.A.: Evolution of human-driven fire regimes in Africa. Proc. Nat. Acad. Sci. 109, 847-852, doi: 10.1073/pnas.1118648109, 2012.

Aurela, M., Beukes, J.P., van Zyl, P., Vakkari, V., Teinilä, K., Saarikoski, S., Laakso, L.: The composition of ambient and fresh biomass: burning aerosols at a savannah site, South Africa. South Afr. J. Sci. 112, 1-8, doi: 10.17159/ sajs.2016/20150223, 2016.

Barrière, J., Oth, A., Theys, N., d'Oreye, N., Kervyn, F.: Long-term monitoring of long-period seismicity and space-based SO_2 observation at African lava lake volcanoes Nyiarango and Nyamulagira (DR Congo). Grophys. Res. Let. 44, 6020-6029, doi: 10.1002/2017GL073348, 2017.

Bauer, S.E., Im, U., Mezuman, K., Gao, C.Y.: Desert dust, industrialization, and agricultural fires: health impacts of outdoor air pollution in Africa. J. Geophys. Res. 124, 4104-4120, doi: 10.1029/2018JD029336, 2019.

Bender, M.M.: Variations in the $^{13}C/^{12}C$ ratios of plants in relation to the pathway of photosynthetic carbon dioxide fixation. Phytochem. 10, 1239-1244, doi: 10.1016.S0031-9422(00)84324-1, 1971.

Bikkina, S., Andersson, A., Sarin, M.M., Sheesley, R.J., Kirillova, E., Rengarajan, R., Sudheer, A.K., Ram, K., Gustafsson, Ö.: Dual isotope characterization of total organic carbon in wintertime carbonaceous aerosols for northern India. J. Geophys. Res. 121, doi: 10.1002/2016JD024880, 2016.

Billmark, K.A., Swap, R.A., Macko, S.A.: Stable isotope and GC/MS characterization African aerosols. South African J. Sci. 101, 177-170, 2005.

Birch, M.E., Cary, R.A.: Elemental carbon-based method for monitoring occupational exposures to particulate diesel exhaust. Aerosol Sci. Technol 25, doi: 10.1080/02786829608965393, 1996.

Bird, M.I., Cali, J.A.: A million-year record of fire in sub-Saharan Africa. Nature 394, 767-769, doi: 10.1038/29507, 1998.

Blanchard, D.C., Woodcock, A. H.: The production, concentration, and vertical distribution of the sea-salt aerosol. Annal. N.Y. Acad. Sci. doi: 10.1111/j.1749-6632.1980.tb17130.x, 1980.

Bond, T.C., Doherty, S.J., Fahey, D.W., Forster, P.M., Berntsen, T., DeAngelo, B.J., Flanner, M.G., Ghan, S., Kärcher, B., Koch, D., Kinne, S., Kondo, Y., Quinn, P.K., Sarofim, M.C., Schultz, M.G., Schultz, M., Venkataram, C., Zhang, H., Zhang, S., Bellouin, N., Guttikunda, S.K., Hopke, P.K., Jacbonson, M.Z., Kaiser, J.W., Klimont, Z., Lohmann, U., Schwarz, J.P., Shindell, D., Storelvmo, T., Warren, S.G., Zender, C.S.: Bounding the role of black carbon in the climate system: A systematic assessment. J. Geophys. Res. 118, 5380-5552, doi: 10.1002./jgrd.50171, 2013.

Brandt, M., Rasmussen, K., Penuelas, Tian, F., J., Schurgers, G., Verger, A., Mertz, O., Palerm, J.R.B., Fensholt, R.: Human population growth offsets climate-driven increase in woody vegetation in sub-Saharan Africa. Nature Ecol. Evol. 1, doi: 10.1038/s41559-017-0081, 2017.

Brito, J., Freney, E., Dominutti, P., Borbon, A., Haslett, S.L., Batenburg, A.M., Colomb, A., Dupuy, R., Denjean, C., Burnet, F., Bourriane, T., Deroubaix, A., Sellegri, K., Borrmann, S. Coe,

544   H., Flamant, C., Knippertz, P., Schwarzenboeck, A.: Assessing the role of anthropogenic and

545   biogenic source on PM1 over southern West Africa using aircraft measurements. Atmos. Chem.

546   Phys. 18, 757-772, doi: 10.5194/acp-18-757-2018, 2018.

547   Cachier, H., Buat-Menard, P., Fontuge, M., Ranhcer, J.: Source terms and source strengths of the

548   carbonaceous aerosol in the tropics. J. Atmos. Chem. 3, 469-489, doi: 10.1007/BF00053872, 1985.

549   Cahoon, D.R., Stocks, B.J., Levine, J.S., Cofer III, W.R., O'Neil, K.P.: Seasonal distribution of

550   African savanna fires. Nature, 359, 812-815, doi: 10.1038/359812a0 , 1992.

551   Cais, P., Bombelli, A., Williams, M., Piao, S.L., Chave, J., Ryan, C.M., Henry, M., Brender, P.,

552   Valentini, R.: The carbon balance of Africa: synthesis of recent research studies. Phil. Trans. Roy.

553   Soc. A 369, 2038-2057, doi: 10.1098/rsta.2010.0328, 2011.

554   Das, O., Wang, Y., Hsieh, Y.-P.: Chemical and carbon isotopic characteristics of ash and smoke

555   derived from burning of C3 and C4 grasses. Org. Geochem. 41, 263-269,

556   10.1016/j.orggeochem.2009.11.001, 2010.

557   Dasari, S., Andersson, A., Bikkina, S., Holmstrand, H., Budhavant, K., Sateesh, S., Asmi, E.,

558   Kesti, J., Backman, J., Salam, A., Singh Bisht, D., Tiwari, S., Hameed, S., Gustafsson, Ö.:

559   Photochemical degradation affects the light absorption of water-soluble brown carbon in the South

560   Asian outflow. Sci. Adv. 5, doi: 10.1126/sciadv.aau8066, 2019.

561   DeWitt, H.L., Gasore, J., Rupakheti, M., Potter, K.E., Prinn, R.G., Ndikubwimana, JdD., Nkusi,

562   J., Safari, B.: Seasonal and diurnal variability in O3, black carbon, and CO measured at the Rwanda

563   Climate Observatory. Atmos. Chem. Phys, 19, 2063-2078, doi: 10.5194/acp-19-2063-201, 2019.

564   Fang, W., Andersson, A., Zheng, M., Lee, M., Holmstrand, H., Kim, S-W., Du, K., Gustafsson,

565   Ö.: Divergent evolution of carbonaceous aerosols during dispersal of East Asian haze. Sc. Rep. 7,

566   doi: 10.1038/s41598-017-10766-4, 2017.

567   Formenti, P., Elbert, W., Maenhaut, W., Haywood, J., Osborne, S., Andreae, M.O.: Inorganic and

568   carbonaceous aerosols during the Southern African Regional Science Initiative (SAFARI 2000)

569 experiment: Chemical characteristics, physical properties, and emission data for smoke from
570 African biomass burning. J. Geophys. Res. 108. Doie: 10.1029/2002JD002408, 2003.

571 Gao, S., Hegg, D.A., Hobbs, P.V., Kirchstetter, T.W., Magi, B.I., Sadilek, M.: Water-soluble
572 organic components in aerosols associated with savanna fires in southern Africa: Identification,
573 evolution and distribution. J. Geophys. Res. 108, doi: 10.1029/2002JD002324, 2003.

574 Gatari, M.J., Boman, J.: Black carbon and total carbon measurements at urban and ruralt sites in
575 Kenya, East Africa. Atmos. Environ. 8, 1149-1154, doi: 10.1016/S1352-2310(02)01001-4, 2003.

576 Graven, H.: Impact of fossil fuel emissions on atmospheric radiocarbon and various applications
577 of radiocarbon over this century. Proc. Nat. Acad. Sci. 112, 9542-9545, doi:
578 10.1073/pnas.1504467112, 2015.

579 Gustafsson, Ö., Kruså, M., Zencak, Z., Sheesley, R.J., Granat, L., Engström, E., Praveen, P.S.,
580 Rao, P.S.P., Leck, C., Rodhe, H.: Brown clouds over South Asia: Biomass or fossil fuel
581 combustion? Science 323, 495-498, doi: 10.1126/science.1164857, 2009.

582 Heft-Neal, S., Burney, J., Bendavid, E., Burke, M.: Robust relationship between air quality and
583 infant mortality in Africa. Nature 559, 254-258, doi: 10.1038/s41586-018-0263-3, 2018.

584 Hodnebrog, Ø., Myhre, G., Forster, P.M., Sillman, J., Samset, B.H.: Local biomass burning is a
585 dominant cause of the observed precipitation reduction in southern Africa. Nature Com. 7, doi:
586 10.1038/ncomms11236, 2015.

587 IPCC – Inter-Governmental Panel for Climate Change: AR5 Climate Change 2013: The physical
588 science basis. ISBN 978-1107661820, 2013.

589 IPCC – Inter-Governmental Panel for Climate Change: AR5 Climate Change 2014: Impacts,
590 adaptation and vulnerability. ISBN 978-1-107-68386-0, 2014.

591 Keeling, C.D.: The concentration and isotopic abundances of atmospheric carbon dioxide in rural
592 areas. Geochem. Cosmochim. Acta. 13, 322-334, doi: 10.1016/0016-7037(58)90033-4, 1958.

593 Kirchstetter, T.W., Novakov, T., Hobbes, P.V., Magi, B.: Airborne measurements of carbonaceous
594 aerosols in southern Africa during the dry biomass season. J. Geophys. Res. 108. Doi:
595 10.1029/2002JD002171, 2003.

596 Kirillova, E.N., Andersson, A., Sheesley, R.J., Kruså, M., Praveen, P.S., Budhavant, K., Safai,
597 P.D., Rao, P.S.P., Gustafsson Ö: ^{13}C and ^{14}C-based study of sources and atmospheric processing
598 of water-soluble organic carbon (WSOC) in South Asian aerosols. J. Geophys. Res. 118, 621-626,
599 doi: 10.1002/jgrd.50130, 2013.

600 Kirillova, E.N., Andersson, A., Han, J., Lee, M., Gustafsson, Ö.: Sources and light absorption of
601 water-soluble organic carbon aerosols in the outflow from northern China. Atmos. Chem. Phys.
602 14, 1413-1422, doi: 10.5194/acp-14-1413-2014, 2014.

603 Kulmala, M.: Build a global Earth Observatory. Nature 553, 21-23, 2018.

604 Liousse, C., Assamoi, E., Criqui, C., Rosset, R.: Explosive growth in African combustion
605 emissions from 2005 to 2030. Environ. Res. Lett. 9, doi: 10.1088/1748-9326/9/3/035003, 2014.

606 Lipset-Moore, G.J., Wolff, N., Game, E.T.: Emissions mitigation opportunities for savanna
607 countries from early dry season fire management. Nature Com. 9, doi: 10.1038/s41467-018-
608 04687-7, 2018.

609 Lloyd, J., Bird, M.I., Vellen, L., Miranda, A.C., Veenendaal, E.M., Djagbletey, G., Miranda, H.S.,
610 Cook, G., Faruqhar, G.D.: Contributions of woody and herbacoues vegetation to tropical savanna
611 ecosystem productivity: a quasi-global estimate. Tree Phys. 28, 451-468, doi:
612 10.1093/treephys/28.3.45, 2008.

613 López-Ballesteros, A:, Beck, J., Bombelli, A., Grieco, E., Lorenkova, E.K., Merbold, L.,
614 Brümmer, C:, Hugo, W., Scholes, R., Vackar, D., Vermeulen, A., Acosta, M., Butterbach-Bahl,
615 K., Helmschrot, J., Kim, D.-G., Jones, M., Jorch, V., Pavleka, M., Skjelvan,I., Saunders, M.:
616 Towards a feasible and representative pan-African research infrastructure network for GHG
617 observations. Environ. Res. Lett. 13, doi: 10.1088/1748-9326/aad66c, 2018.

618 Maenhaut, W., Salma, I., Cafmeyer, J., Annegarn, H.J., Andreae, M.O.: Regional atmospheric
619 aerosols composition and sources in the eastern Transvaal, South Africa, and impact of biomass
620 burning. J. Geophys. Res. 101, 23631-23650, 1996.

621 Martens, J., Wild, B., Pearce, C., Tesi. T., Andersson, A., Bröder, L., O'Regan, M., Jakonsson,
622 M., Sköld, M., Gemery, L., Cronin, T.M., Semiletov, I., Dudarev, O.V., Gustafsson, Ö.: (2019)

Remobilization of Old Permafrost Carbon to Chukchi Sea Sediments During the End of the Last Deglaciation. Glob. Biogeochem. Cyc. 33, 2-14, doi: 10.1029/2018GB005969.

Martinelli, L.A., Camargo, P.B., Lara, L.B.L.S., Victoria, R.L., Artaxo, P.: Stable carbon and nitrogen isotopic composition of bulk aerosol particles in a C4 plant landscape of southeast Brazil. Atmos. Environ. 36, 2427-2432, doi: 10.1016/S1352-2310(01)00454-X, 2002.

Marwick, T.R., Tamooh, F., Teofuru, C.R., Borget, A.V:, Darchambeau, F., Bouillon, S.: The age of river-transported carbon: global perspective. Glob. Biogeochem. Cyc. 29, 122-137, doi: 10.1002/2014GB004911, 2015.

Mkoma, S.L., Kawamura, K., Tachibana, E., Fu, P.: Stable carbon and nitrogen isotopic compositions of tropical atmospheric aerosols: sources and contribution from burning of C_3 and C_4 plants to organic aerosols. Tellus B, 66, 1-12, doi: 10.3402/tellusb.v66.20176, 2014.¨

O'Leary, M.H.: Carbon isotopes in photosynthesis. Bioscience 38, 328–36, doi: 10.2307/1310735, 1988.

Palmer, P.I., Feng, L., Chevallier, F., Bösch, H., Somkuti, P.: Net carbon emissions from African biosphere dominate pan-tropical atmospheric CO_2 signal. Nature Com. 10. doi: 10.1038/s41467-019-11097-w, 2019.

Puxbaum, H., Rendl, J., Allabashi, R., Otter, L., Scholes, M.C.: Mass balance of the atmospheric aerosol in a South African savanna (Nylsvley, May 1997). J. Geophys. Res. 105, 20697-20706, 2000.

Roberts, G.O., Gelman, A., Gilks, W.R.: (1997) Weak convergence and optimal scaling of random walk Metropolis algorithms. Ann. Appl. Prob. 7, 110-120.Sheesley, R.J., Kirllova, E.N., Andersson, A., Kruså, M., Praveen, P.S., Budhavant, K., Safai, P.D., Rao, P.S.P., Gustafsson, Ö.: Year-round radiocarbon-based source apportionment of carbonaceous aerosols at two background sites in South Asia. J. Geophys. Res. 117, doi: 10.1029/2011JD017161, 2012.

Sinha, P., Hobbs, P.V., Yokelson, R.J., Bertschi, I.T., Blake, D.R., Simpson, I.J., Gao, S., Kirchstetter, T.W., Novakov, T.: Emissions of trace gases and particles from savanna fires in southern Africa. J. Geophys. Res. 108, doi: 10.1029/2002JD002325, 2003.

650 Swap, R.J., Annegard, H.J., Suttles, J.T., King, M.D., Platnick, S., Privette, J.L., Scholes, R.J.:
651 Africa burning: A thematic analysis of the Southern African regional science initiative (SAFARI
652 2000). J. Geophys. Res. 108, doi: 10.1029/2003JD003747, 2003.

653 Tiitta, P., Vakkari, V., Croteau, P., Beukes, J.P., van Zyl, P.G., Josipovic, M., Venter, A.D., Jaaros,
654 K., Pienaar, J.J., Ng, N.L., Canagaratna, M.R:, Jayne, J.T., Kerminen, V.-K., Kokola, H., Kulmala,
655 M., Laaksonen, A., Worsnop, D.R., Laakso, L.: Chemical composition, main sources and temporal
656 variability of PM1 aerosols in southern African grassland. Atmos. Chem. Phys. 14, 1909-1927,
657 doi: 10.5194/acp-14-1909-2014, 2014.

658 Turekian, V. C., Macko, S., Swap, R. J. and Garstang, M.: Causes of bulk carbon and nitrogen
659 isotopic fractionations in the products of vegetation burns: laboratory studies. Chem. Geol. 152,
660 181-192, 10.1016/S0009-2541(98)00105-3, 1998.

661 Turnbull, J.C., Mikaloff Fletcher, S.E., Ansell, I., Brailsford, G.W., Moss, R.C., Norris, M.W.,
662 Steinkamp, K.: Sixty years of radiocarbon dioxide measurements at Wellington, New Zealand:
663 1965-2014. Atmos. Chem. Phys. 17, 14771-14784, doi: 10.5194/acp-17-14771-2017, 2017.

664 UNDP – United Nations Development Programme: 2018 Africa Sustainable Development Report:
665 Towards a transformed and resilient continent. ISBN: 978-92-1-125134-0, 2018.

666 UNEP/WMO – United Nations Environment Programme/World Meteorological Organization:
667 Integrated assessment of black carbon and tropospheric ozone. ISBN: 978-92-807-3142-2, 2012.

668 Valentini, R., Arneth, A., Bombelli, A., Castaldi, S., Cazzolla Gatti, R., Chevallier, F., Cias, P.,
669 Grieco, E., Hartmann, J., Henry, M., Houghton, R.A., Jung, M., Kutsch, W.L., Malhi, Y.,
670 Mayorga, E., Merbold, L., Murray-Tortarolo, G., Papale, D., Peylin, P., Poulter, B:, Raymond,
671 P.A., Santini, M., Sitch, S., Vaglio Laurin, G., van der Werf, G.R., Williams, C.A., Scholes, R.J.:
672 A full greenhouse gases budget of Africa: synthesis, uncertainties, and vulnerabilities.
673 Biogeosciences 11, 381-407, doi: 10.5194/bg-11-381-2014, 2014.

674 WHO – World Health Organization: Health effects of black carbon. ISBN: 978 92 890 0265 3,
675 2012.

676   WHO – World Health Organization: Ambient air pollution: A global assessment of exposure and
677   burden of disease. ISBN: 9789241511353, 2016.

678   Widory, D.: Combustibles, fuels and their combustion products: A view through carbon isotopes.
679   Combust. Theory Mod. 10, 831-841, doi: 10.1080/13647830600720264, 2006.

680   Wild, B., Andersson, A., Bröder, L., Vonk, J:, Hugelius, G., McClelland, J.W., Song, W.,
681   Raymond, P.A., Gustafsson, Ö.: Rivers across the Siberian Arctic unearth the patterns of carbon
682   release from thawing permafrost. Proc. Nat. Acad. 116, 10280-10285, doi:
683   10.1073/pnas.181179116, 2019.

684   Williams, C.A., Hanan, N.P., Neff, J.C., Scholes, R.J., Berry, J.A., Denning, S.A., Baker, D.F.:
685   Africa and the global carbon cycle. Carbon Bal. Manag. 2, 1-13, doi: 10.1186/1750-0680-2-3,
686   2007.

687   Winiger, P., Andersson, A., Eckhardt, S., Stohl, A., Semiletov, I.P., Dudarev, O.V., Charkin, A.,
688   Shakova, N., Klimont, Z., Heyes, C., Gustafsson, Ö.: (2017) Siberian Arctic black carbon sources
689   constrained by model and observation. Proc. Nat. Acad. Sci. doi: 10.1073/pnas.1613401114.

690   Winiger, P., Barrett, T.E., Sheesley, R.J:, Huang, L., Sharma, S., Barrie, L.A., Yttri, K.E.,
691   Evangeliou, N., Eckhardt, S., Stohl, A., Klimont, Z., Heyes, C., Semiletov, I.P., Dudarev, O.V.,
692   Charkin, A., Shakhova, N., Holmstrand, H., Andersson, A., Gustafsson, Ö.: Source apportionment
693   of circum-Arctic atmospheric black carbon from isotopes and modelling. Sci. Adv. 5, doi:
694   10.1126/sciadv.aau8052, 2019.

695   Yan, C., Zheng, M., Bosch, C., Andersson, A., Desyaterik, Y., Sullivan, A.P., Collett, J.L., Zhao,
696   B., Wang, S., He, K., Gustafsson, Ö.: Important fossil source contribution to brown carbon in
697   Beijing during Winter. Sci. Rep. 7, doi: 10.1038/srep43182, 2017.

TABLES

Table 1. Concentrations of carbonaceous aerosol ($\mu g C\ m^{-3}$) and inorganic ions ($\mu g\ m^{-3}$) in fine aerosols from ground-based and airborne measurements over Sub-Saharan Africa (bkg = background).

Sampling site	TC	OC	BC/EC	WSOC	NO_3^-	SO_4^{2-}	NH_4^+	K^+
RCO, dry[a]	9.5±3.7	8.2±3.2	1.3±0.6	5.7±2.1	1.2±0.7	2.1±1.0	0.8±0.3	0.7±0.3
RCO, wet[a]	2.4±1.2	2.2±1.1	0.20±0.1	1.5±0.7	0.1±0.1	0.7±0.3	0.3±0.1	0.08±0.05
Rural Tanzania, dry[b]	7±2	6±2	1.0±0.3	4±1	0.18±0.06	0.2±0.1	0.9±0.7	1.5±0.7
Rural Tanzania, wet[b]	4±1	4±1	0.5±1.3	3±1	0.06±0.03	0.1±0.1	0.2±0.1	0.4±0.2
Aircraft, Southern Africa, smoke[c]	N/A	N/A	N/A	N/A	4.84±0.02	10.4±0.6	N/A	13.1±0.1
Aircraft, Southern Africa, bkg[c]	N/A	N/A	N/A	N/A	0.48±0.00	2.2±0.1	N/A	0.31±0.02
Aircraft, Southern Africa fresh[d]	N/A	20±18	2±1	N/A	1.4±1.8	1.9±1.4	1.6±2.4	4.5±8.1
Aircraft, Southern Africa aged[d]	N/A	6±3	1.03±0.04	N/A	1.0±0.8	2.0±1.5	0.9±0.8	0.6±0.4
Aircraft, Southern Africa, plume[e]	106±86	91±74	15±12	N/A	N/A	N/A	N/A	N/A
Aircraft, Southern Africa haze[e]	10.5±8.2	9.5±6.8	2.3±1.8	N/A	N/A	N/A	N/A	N/A
Aircraft, Southern Africa[f]	8.5±4.8	N/A	2.3±1.9	N/A	0.8±0.3	4.5±3.6	N/A	0.4±0.1
National Park, South Africa[g]	N/A	N/A	1.2 - 2.2	N/A	N/A	N/A	N/A	0.22 - 0.34
Savanna, South Africa[h]	9.1	N/A	0.61	N/A	0.4	11.08	2.85	0.28
Aircraft, W. Africa, bkg[i]	N/A	N/A	0.33 – 0.35	N/A	0.11 – 0.12	1.64 – 1.70	0.63 – 0.68	N/A
Aircraft, W. Africa, urban plume[i]	N/A	N/A	0.64 – 0.72	N/A	0.49 – 0.53	2.70 – 3.03	1.20 – 1.38	N/A
Grassland, South Africa, dry[j]	N/A	N/A	0.6	N/A	0.3	1.4	0.2	N/A
Grassland, South Africa, wet[j]	N/A	N/A	0.3	N/A	0.2	0.4	0.3	N/A
Savanna, South Africa, spring[k]	N/A	N/A	0.40	N/A	0.05	2.48	0.05	0.17
Savanna, South Africa, summer[k]	N/A	N/A	0.16	N/A	0.01	5.65	0.01	0.2

a. Present study
b. Mkoma et al., 2014
c. Gao et al., 2003
d. Formenti et al., 2003
e. Kirchstetter et al, 2003
f. Sinha et al., 2003
g. Maenhaut et al., 1996
h. Puxbaum et al., 2000
i. Brito et al., 2018
j. Tiitta et al., 2014
k. Aurela et al., 2016

713 **FIGURES**
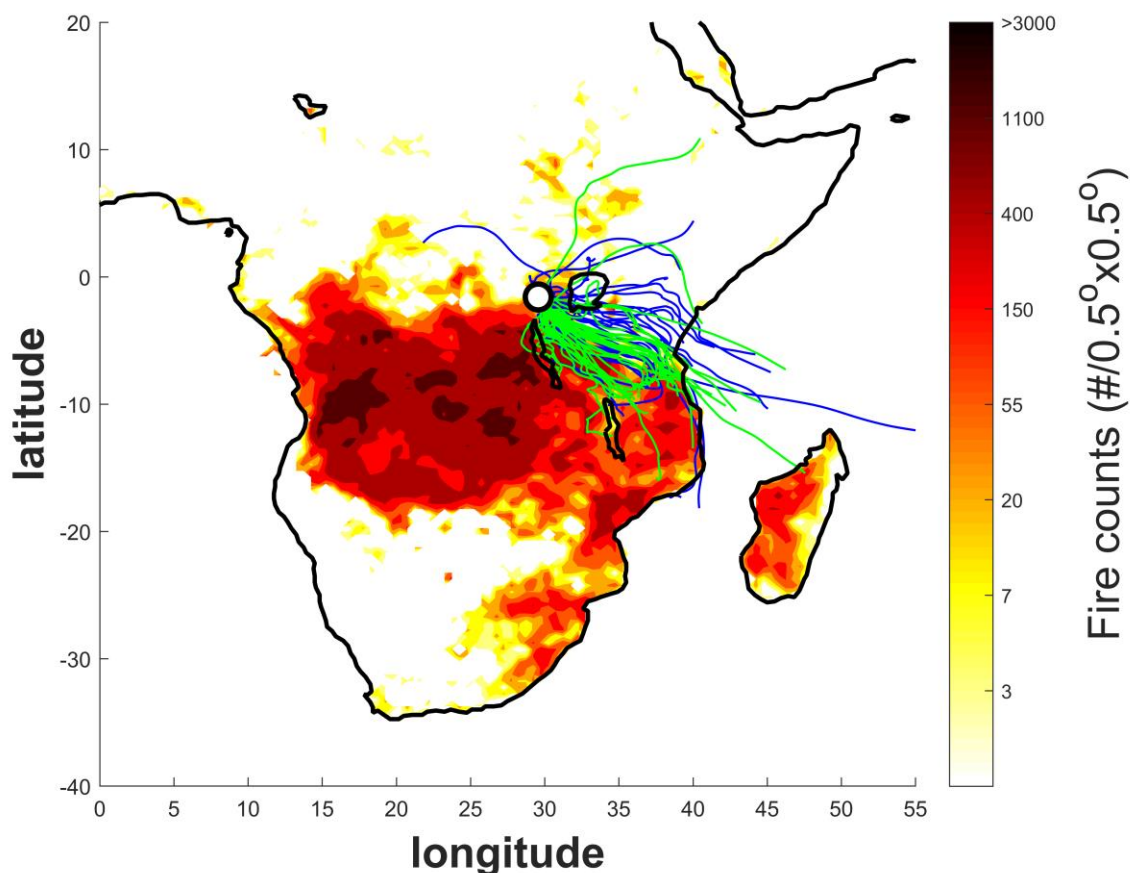
714

715 **Figure 1** Fire counts and air mass back trajectories for the October 2014 to September 2015
716 campaign at the Rwanda Climate Observatory (RCO, black and white circle). The fire counts are
717 from the Fire Information for Resource Management System (FIRMS) derived from the NASA
718 Moderate Resolution Imaging Spectroradiometer (MODIS) satellite product for June-July-August
719 (JJA), 2015. The thin lines represent (4AM, C.A.T.) 5-day air mass back-trajectories arriving at
720 RCO 100 m.a.g.l. (2690 m.a.s.l.). The blue lines correspond to what we here refer to as the 'wet'
721 seasons (October-November 2014 and April-May 2015), whereas the green lines represent the dry
722 JJA season.

723

724

725
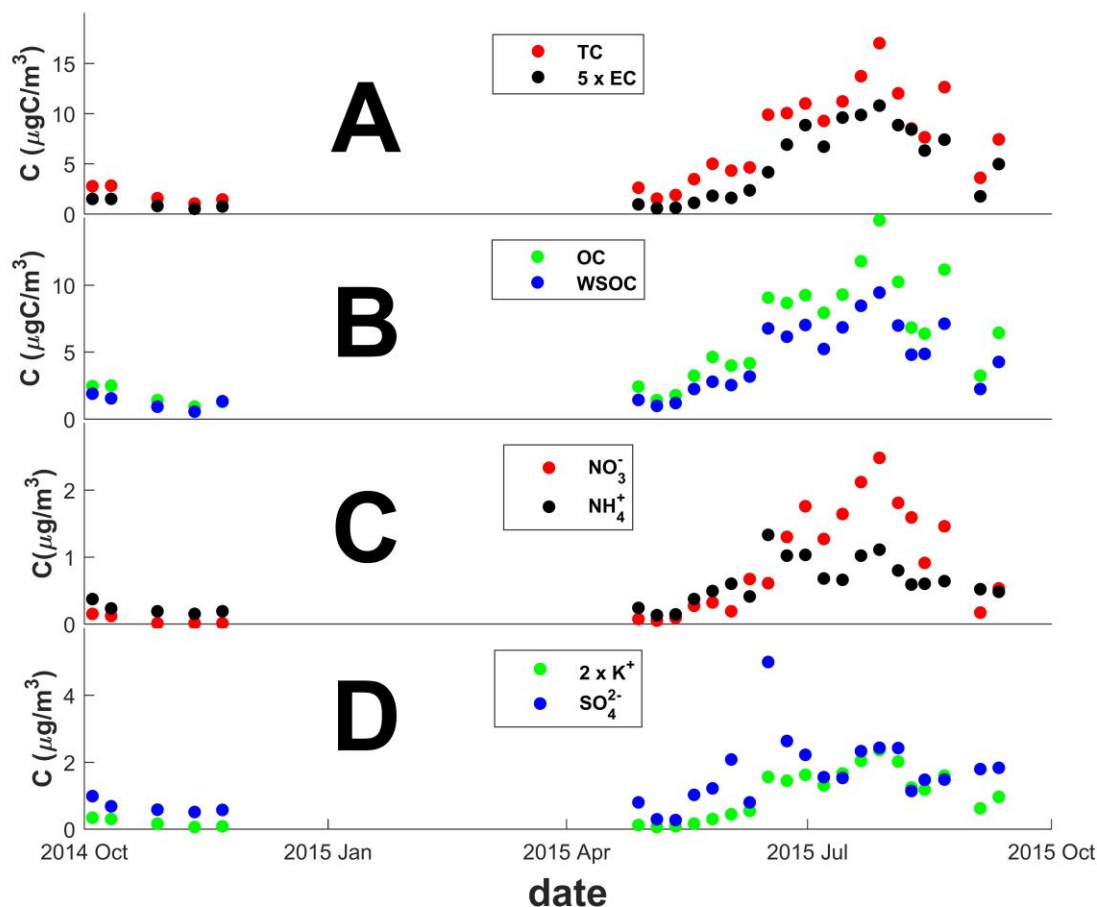
Figure 2. Time-dependence of concentrations of carbonaceous aerosols (TC = total carbon; EC = elemental carbon; OC = organic carbon; WSOC = water-soluble organic carbon) and inorganic ions in PM$_{2.5}$ during October 2014 to September 2015 at the Rwanda Climate Observatory. Panel A. TC and EC. Panel B. OC and WSOC. Panel C. NO$_3^-$ and NH$_4^+$. Panel D. K$^+$ and SO$_4^{2-}$. Instruments were hit by lightning resulting in a data gap November 2014 to April 2015. The concentrations of EC were multiplied by 5 and K$^+$ by 2 for visual clarity.

732
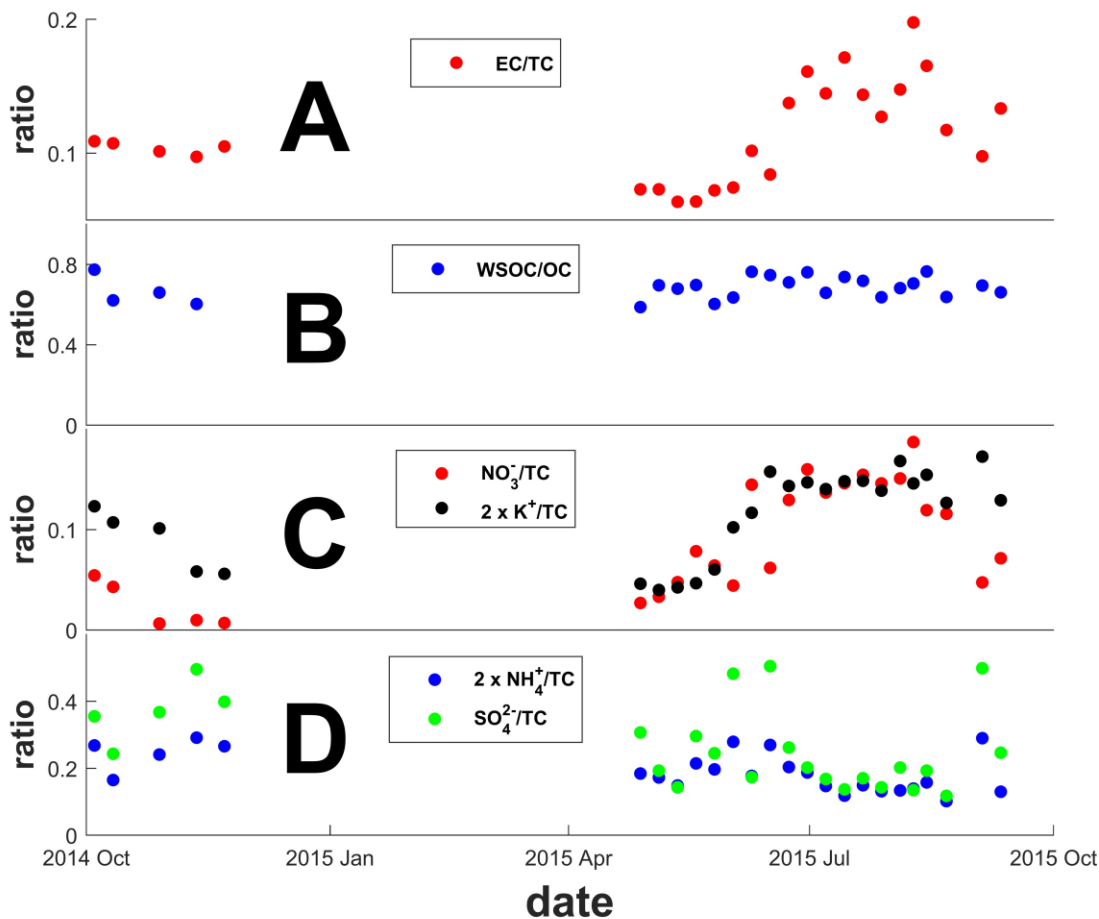
Figure 3. Time-dependence of ratios of carbonaceous aerosols (EC = elemental carbon; OC = organic carbon; WSOC = water-soluble organic carbon) and inorganic ions relative to total carbon (TC) in $PM_{2.5}$ during October 2014 to September 2015 at the Rwanda Climate Observatory. Panel A. EC/TC. Panel B. WSOC/OC. Panel C. NO_3^-/TC and K^+/TC. Panel D. NH_4^+/TC and SO_4^{2-}/TC. Instruments were hit by lightning resulting in a data gap November 2014 to April 2015. The concentrations of K^+/TC and NH_4^+/TC ratios were multiplied by 2 for visual clarity.

739
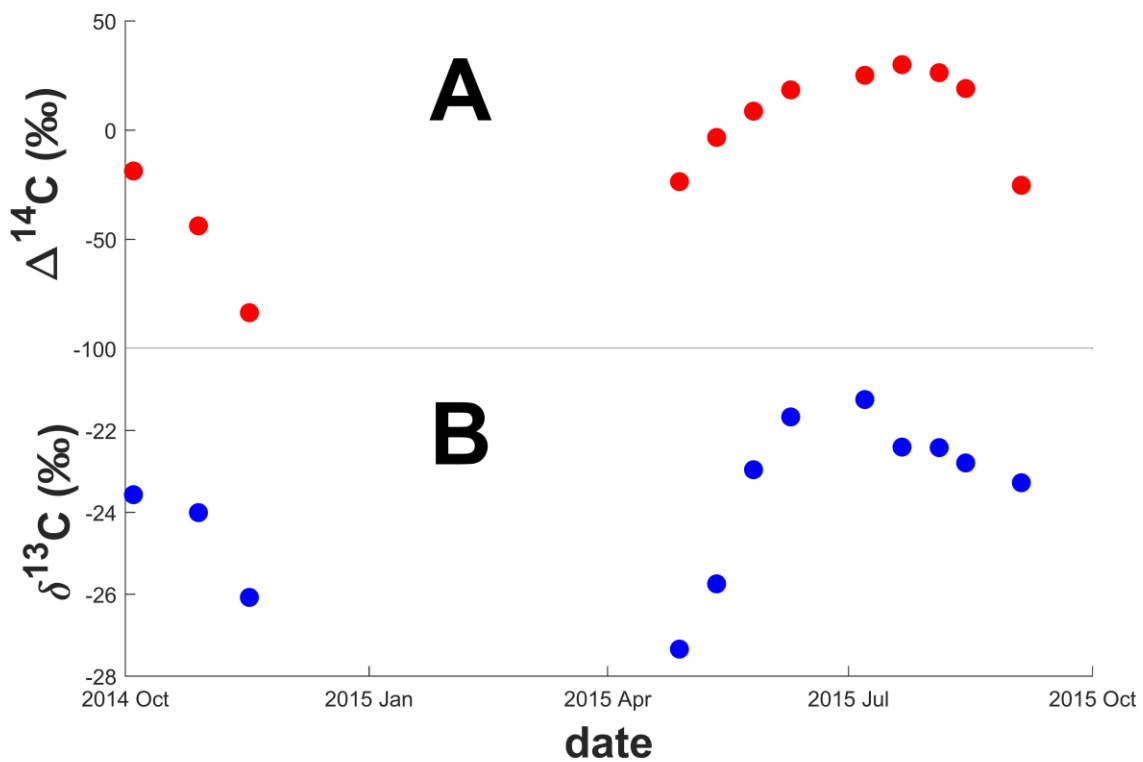
740

741 **Figure 4**: Dual carbon isotope data for TC vs time. Panel A. Δ^{14}C and Panel B. δ^{13}C. The
742 uncertainties for Δ^{14}C are below 50‰ and ~ 0.2‰ for δ^{13}C. Instruments were hit by lightning
743 resulting in a data gap November 2014 to April 2015.

744
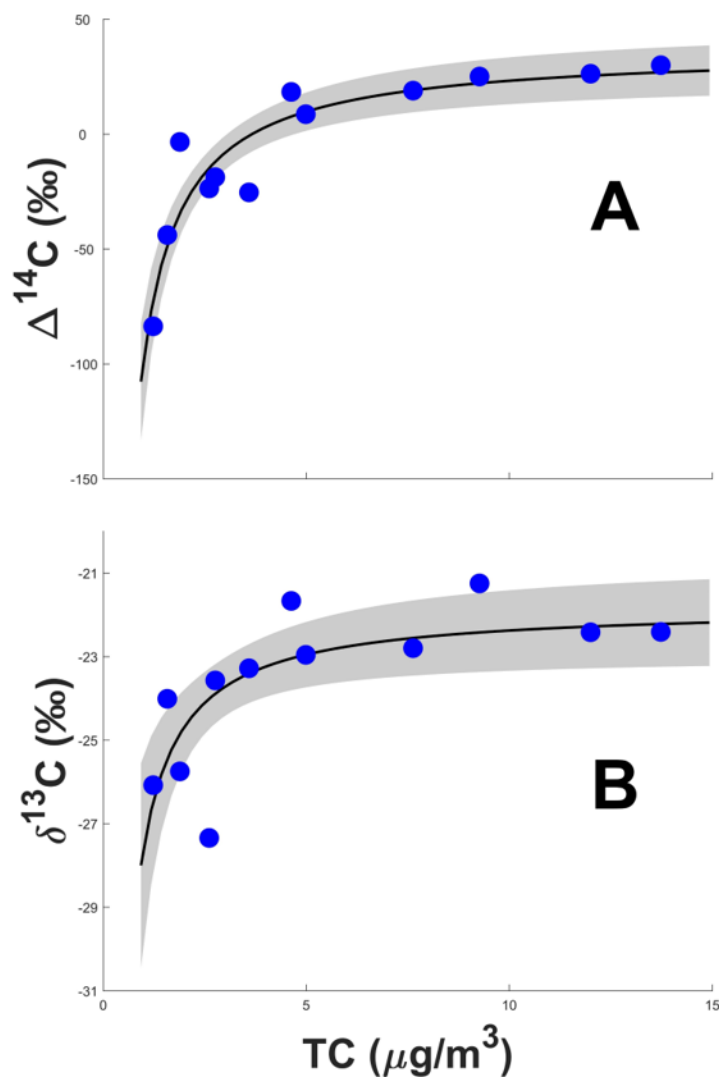
Figure 5. Interrelations of carbon isotope signatures and TC (blue circles). Panel A. Δ^{14}C vs TC, Panel B. δ^{13}C vs TC. The black line is the mean fit of the equation Δ^{14}C, δ^{13}C = A/[TC]+B, using Markov chain Monte Carlo simulations, where A and B are fitting parameters. For Δ^{14}C, A= -135±16 ‰ µg m^{-3}; B= 37±6 ‰. For δ^{13}C, A= -5.8±1.5 ‰; B= -21.8±0.6 ‰ µg m^{-3}. The grey shaded area display the 1σ spread of the fit.

750
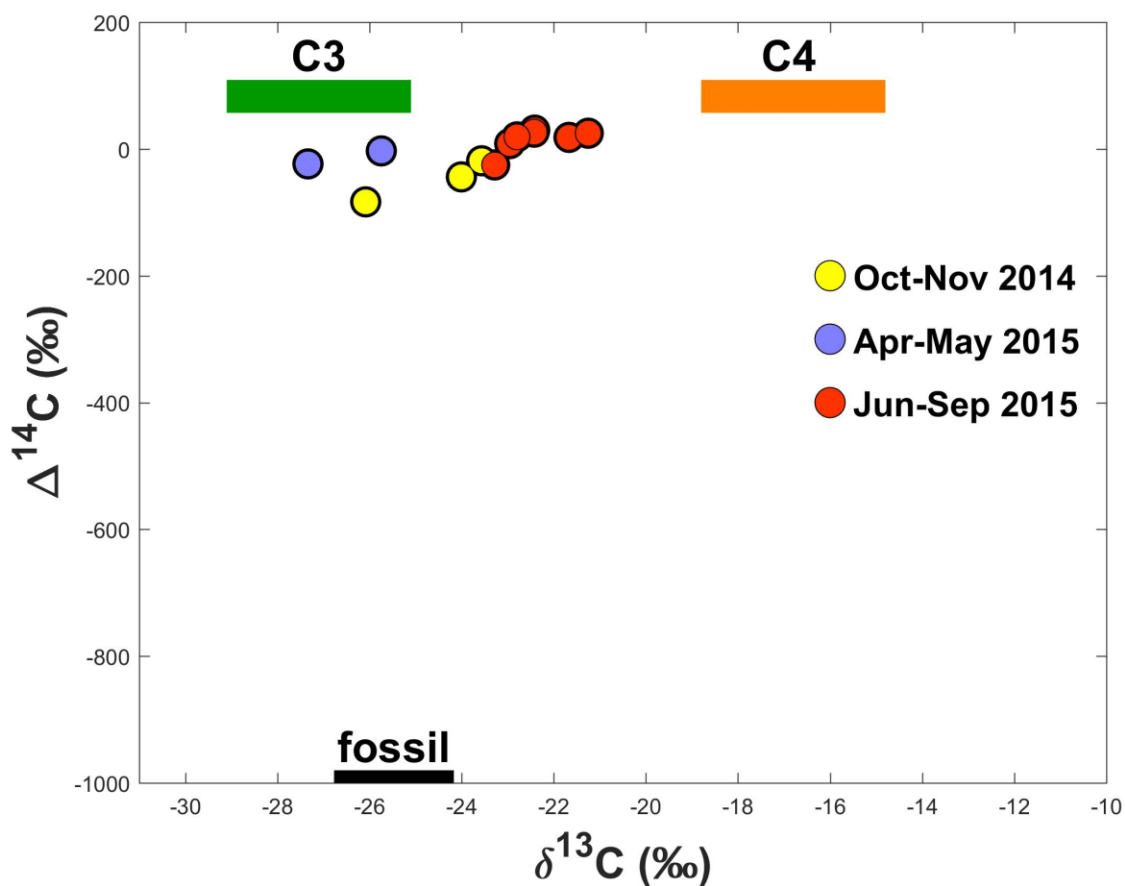
Figure 6: Dual carbon (Δ^{14}C vs δ^{13}C) isotope plot of TC. Blue circles represent Oct-Nov 2014 (wet), yellow circles Apr-May 2015 (wet), and red circles Jun-Sept 2015 (dry). The boxes represent the endmember ranges (mean ± stdev; see Section 3.5 for details) of the three main sources: C$_3$-plants (green), C$_4$-plants (orange), and fossil (black).

755

756

757

758
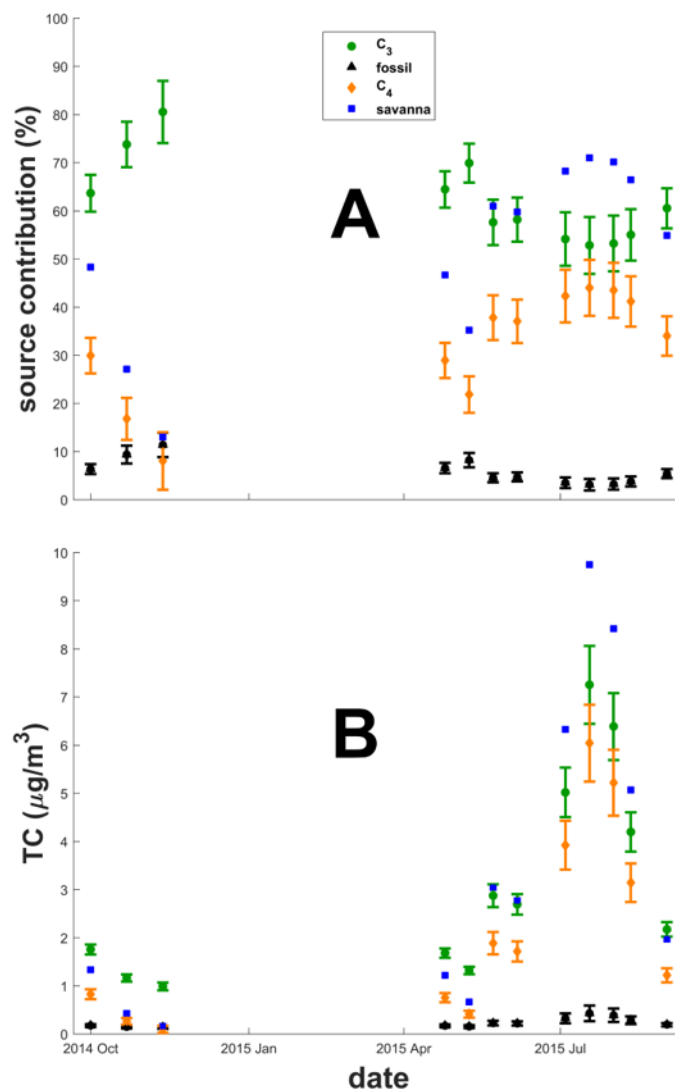
Figure 7: Carbon isotope source-segregated fractions and concentrations of TC vs time computed with the 'best endmember scenario'. Panel A. Relative source contributions (%) of C_3-plants (green circles), C_4-plants (orange diamonds) and fossil (black triangles). Estimated savanna contributions are shown as blue squares. Panel B. Source segregated concentrations of TC of C_3-plants (green circles), C_4-plants (orange diamonds) and fossil (black triangles). The error bars (standard deviations) were calculated using Markov chain Monte Carlo simulations.

765